Aharonov–Bohm oscillations, quantum decoherence and amplitude modulation in mesoscopic InGaAs/InAlAs rings

S L Ren[1]**, J J Heremans**[1]**, C K Gaspe**[2]**, S Vijeyaragunathan**[2]**,
T D Mishima**[2] **and M B Santos**[2]

[1] Department of Physics, Virginia Tech, Blacksburg, VA 24061, USA
[2] Homer L Dodge Department of Physics and Astronomy, University of Oklahoma, Norman, OK 73019, USA

E-mail: heremans@vt.edu

Abstract

Low-temperature Aharonov–Bohm oscillations in the magnetoresistance of mesoscopic interferometric rings patterned on an InGaAs/InAlAs heterostructure are investigated for their dependence on excitation current and temperature. The rings have an average radius of 650 nm, and a lithographic arm width of 300 nm, yielding pronounced interference oscillations over a wide range of magnetic fields. Apart from a current and temperature dependence, the oscillation amplitude also shows a quasi-periodic modulation with applied magnetic field. The phase coherence length is extracted by analysis of the fundamental and higher Fourier components of the oscillations, and by direct analysis of the amplitude and its dependence on parameters. It is concluded that the Thouless energy forms the measure of excitation energies for quantum decoherence. The amplitude modulation finds an explanation in the effect of the magnetic flux threading the finite width of the interferometer arms.

(Some figures may appear in colour only in the online journal)

1. Introduction

The study of quantum phase decoherence in solid-state systems yields insights into the fundamental properties of mesoscopic systems, which are large compared to the atomic scale but still of a length scale preserving quantum phenomena. Understanding quantum decoherence is also important in the field of quantum information processing. Electron quantum interference has become an important method to explore mesoscopic physics and quantum decoherence, using phenomena such as weak-localization and using lithographically fabricated interferometers of a length scale comparable to the phase coherence length l_ϕ at low temperatures (T). In the solid-state, several types of interferometers have proved amenable to fabrication at the mesoscopic scale using advanced nanolithographic techniques, such as Mach–Zehnder interferometers, Fabry–Perot-type interferometers, and, the type used in this work, Aharonov–Bohm ring interferometers.

One of the more remarkable manifestations of quantum interference is the Aharonov–Bohm (AB) effect [1, 2], not only because it has proved experimentally accessible if care is taken in the preparation of samples, but also, among others, because it forms a main ingredient of magnetoresistance due to localization and mesoscopic phenomena in the solid-state [3, 4] and because it illustrates non-local phenomena in quantum physics and the consequences of gauge invariance. Our measurements are performed in two-dimensional semiconductor heterostructure AB ring electron interferometers, where the magnetoresistance (MR) of the ring exhibits the AB effect: the ring resistance R shows a periodicity in the applied magnetic field B applied normal to the ring. The period of the oscillations in $R(B)$ coincides with the magnetic flux through the ring changing by one flux quantum $\Phi_0 = \frac{h}{e}$, where h is Planck's constant and e is the electron charge [5]. Since B is uniform over the ring area, for our rings of mean radius r the

flux threading the ring is $\Phi(B) = B\pi r^2$, and the period in B of $R(B)$ can be predicted from lithographic sizes.

The phase coherence length l_ϕ is defined as the distance electrons travel before their quantum phase is randomized by inelastic scattering processes, and, at low T, l_ϕ can reach a few micrometers [6]. The amplitude A of the AB oscillations observed in an electron interferometer decays exponentially [7, 8] with the electron path length l, as:

$$A(l) = A_0 \exp(-l/l_\phi) \qquad (1)$$

where A_0 is a prefactor dependent on energy smearing via the thermal energy $k_B T$ (where k_B is the Boltzmann constant) and via a voltage or current bias. For an AB ring, the $\frac{h}{e}$ oscillation period corresponds to a path length $l = \pi r$ and is the strongest component in the frequency spectrum in $R(B)$. A weaker component at $\frac{h}{2e}$ often exists, corresponding to a path length $l = 2\pi r$. Rarely a component at $\frac{h}{3e}$ is observed, corresponding to a path length $l = 3\pi r$. From the experimentally observed amplitudes in the frequency spectrum and using the correspondence between the $\frac{h}{ne}$ mode and the path length $l = n\pi r$, equation (1) allows l_ϕ to be deduced [9]. The mobility mean free path forms another important length scale, limited by elastic momentum scattering processes, and defined as $l_e = v_F \tau_e$, where v_F is the Fermi velocity, $\tau_e = \mu m_e^*/e$ is the momentum relaxation time derived from the mobility μ, and m_e^* represents the electron effective mass ($m_e^* = 0.035 m_e$ at the Γ-point in our system, where m_e represents the free-electron mass). Our rings are in the quasi-ballistic regime, where l_e approximately equals the path length πr, and ballistic, rather than diffusive, expressions are used to describe mesoscopic transport phenomena.

The thermal energy $k_B T$ leads to an uncertainty ΔE in a quantum state's eigenenergy (thermal smearing) and will lead to phase decoherence between electrons, due to a phase difference accumulated over a finite path length L. Equivalently, the excitation voltage V_{exc} generated across a system of resistance R and traversed by an excitation current I, will also lead to an energy smearing $\Delta E = eV_{exc} = eIR$. The critical energy scale for phase decoherence by energy smearing in a finite system is quantified by the Thouless energy [10] E_c, expressing the eigenenergy change that would cause a phase shift of 1 over a path length L:

$$E_c = \frac{\hbar}{\tau} = \frac{\hbar^2 k_F}{m_e^* L} \qquad (2)$$

where $\hbar = h/2\pi$, $\tau = L/v_F$ is the traversal time, and k_F is the Fermi wavevector. For an AB ring, more specifically $L = \pi r$. If $\Delta E > E_c$ then $\Delta E/E_c$ independent and incoherent channels contribute to transport, averaging out the interference signal proportionally to $\sqrt{E_c/\Delta E}$ [5, 11]. For AB oscillations, a reduction in the amplitude prefactor A_0 is expected $\sim \sqrt{E_c/\Delta E}$. ΔE can be determined either by the excitation voltage across the system, using $\Delta E = eV_{exc} = eIR$, or by the temperature T, using $\Delta E = \kappa k_B T$. A value $\kappa > 1$ is expected since averaging occurs if the thermally accessible energy range ΔE is sufficiently wide to give rise to a significant number of statistically independent Thouless energy intervals E_c. We adopt $\kappa \approx 3$, as suggested in [7, p 102].
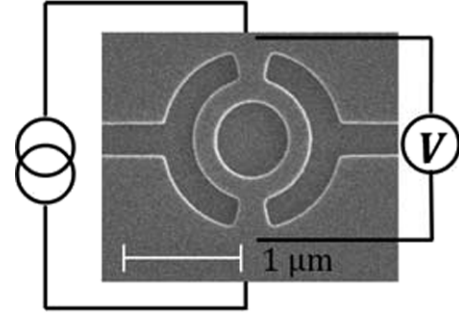

Figure 1. SEM micrograph of a representative Aharonov–Bohm ring, with a schematic of the four-terminal measurement setup. The darker gray areas (delineated by white borders) are etched trenches depleted of electrons, and function as barriers, forcing the electrons to travel into the lighter gray ring-shaped areas.

A modulation of the AB oscillation amplitude with B in mesoscopic systems has been a generally observed phenomenon in experiments [5, 12–20], sometimes ascribed to spin-dependent processes [13–15], or dynamic processes [20]. Recently [12] used an autocorrelation function in B to analyze the modulation, based on the fact that when the magnetic flux through the finite width of the interferometer arms changes by $\sim \Phi_0$, a new realization of the mesoscopic system occurs and the oscillation amplitude and phase are modified. Our modulation data is in good accordance with this view, and this work hence adopts the method in [12]. We also offer an alternative explanation, where different oscillation periods in $R(B)$ occur due to different paths allowed by the finite width of the interferometer arms.

2. Experiments

Figure 1 shows a scanning electron microscope (SEM) micrograph of a representative AB ring fabricated on an $In_{0.64}Ga_{0.36}As/In_{0.45}Al_{0.55}As$ heterostructure by electron-beam lithography and inductively coupled plasma reactive ion etching (ICP-RIE). The heterostructure contains a two-dimensional electron system (2DES) in a 10 nm wide $In_{0.64}Ga_{0.36}As$ quantum well located 50 nm from the surface. The 2DES density $N_S = 9.4 \times 10^{11}$ cm^{-2} (yielding a Fermi wavelength $\lambda_F = 26$ nm) and the mobility $\mu = 5.9 \times 10^4$ cm^2 (V s)$^{-1}$ at 0.4 K, resulting in a 2DES resistivity $\rho_{2D} = 110$ $\Omega/\square$. Taking non-parabolicity of the conduction band into account, the 2DES has $l_e = 1.7$ μm, placing the AB rings in the quasi-ballistic regime. The micrograph depicts a different AB ring from those used in the experiments, but equivalent in layout. Lithographically, the rings in the experiments feature an average radius $r = 650$ nm, arm width $w = 300$ nm (the central antidot has radius 500 nm). The average radius yields an expected AB oscillation period of 31 G. We performed low-frequency ac lock-in four-terminal measurements as indicated in figure 1, applying the ac excitation current I through the AB ring, and detecting the voltage across the AB ring under variable B applied normal to the heterostructure area. The excitation currents I varied from 10 to 300 nA (rms values), with
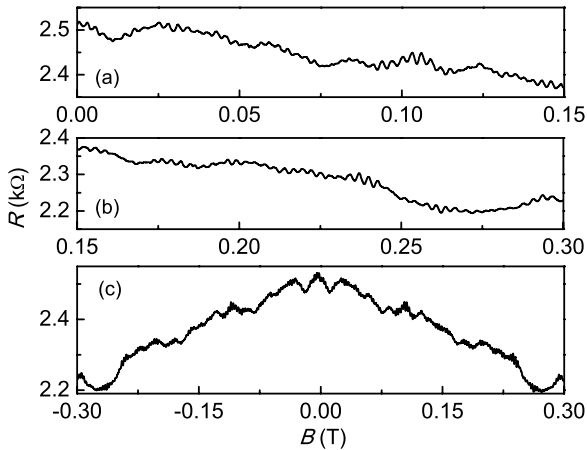
Figure 2. Measured Aharonov–Bohm magnetoresistance oscillations, as ring resistance $R(B)$ versus B. Panels (a) and (b) show the ring magnetoresistance over smaller ranges of B than panel (c), which emphasizes a view of the modulation with B.

T from 0.390 to 3.00 K. Two samples were measured, of nominally identical lithographic design and identically processed, and for each sample several cooldowns and measurements were performed. For a given sample the usual variations were encountered between measurements from different cooldowns, since the magnetotransport fingerprint of mesoscopic systems is delicately dependent on the specific unintentional impurity configuration achieved during the cooldown (via universal conductance fluctuation backgrounds). While the data from each cooldown bears a unique fingerprint, our analysis of the bias and T dependence and of the modulation is not sensitive to such variations, and consistent behavior with respect to our conclusions was observed. For the following discussion, most of the data presented originates from one sample with different cooldowns. Use of data from the second sample is specifically indicated. The typical resistance of an AB ring is 2.5 kΩ at 0.4 K, a value consistently encountered, with variations within 10%.

3. Results and discussion

Pronounced AB oscillations were observed over a wide range of B up to 0.6 T. Below 0.3 T the oscillations are stronger and, as figure 2 shows, display a quasi-periodic modulation with B. Figure 2(c) provides data from -0.3 to 0.3 T, from which the modulation is apparent. Higher resolution is provided in figures 2(a) and (b). Next, we will focus on the lower range of B.

3.1. AB oscillations in low magnetic fields

The low B measurements are performed below 0.06 T. A typical measurement around $B = 0$ is presented in figure 3. Figure 3(a) contains the data as-taken, figure 3(b) shows the same data after background MR subtraction, and figure 3(c) presents the Fourier transform. The Fourier transform displays a maximum at $\sim$400 1/T, labeled as $\frac{h}{e}$, corresponding to the AB oscillations visible in figures 3(a) and (b), and corresponding to the $\frac{h}{e}$ component of the spectrum. A smaller maximum appears at $\sim$800 1/T, corresponding to the $\frac{h}{2e}$ component. The Fourier transform indicates a period in B of 25 G for the $\frac{h}{e}$ component. For a path following the average radius of 650 nm, a period of 31 G is expected for the $\frac{h}{e}$ component. The observed period of 25 G corresponds to a preferred path having an average radius of 730 nm. Accounting for the arm width, such a preferred path lies within expectations, as discussed later in this section.

Figures 3(a) and (b) show that the AB oscillation amplitude varies with a quasi-period of $\sim$200 G, a variation
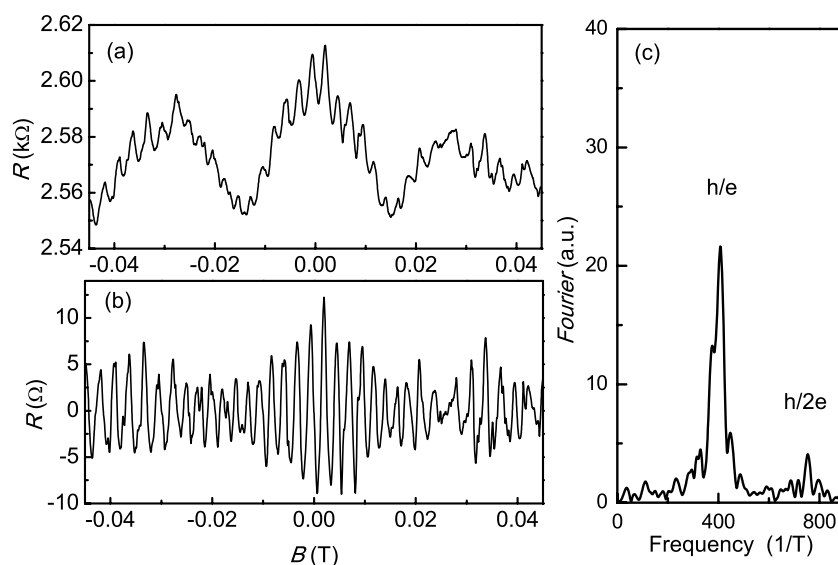

Figure 3. Aharonov–Bohm magnetoresistance oscillations around $B = 0$ at 0.4 K. Panel (a) shows the raw data. Panel (b) shows the data after background removal. Panel (c) contains the Fourier transform of (b), where $\frac{h}{e}$ and $\frac{h}{2e}$ modes are indicated in the frequency spectrum.
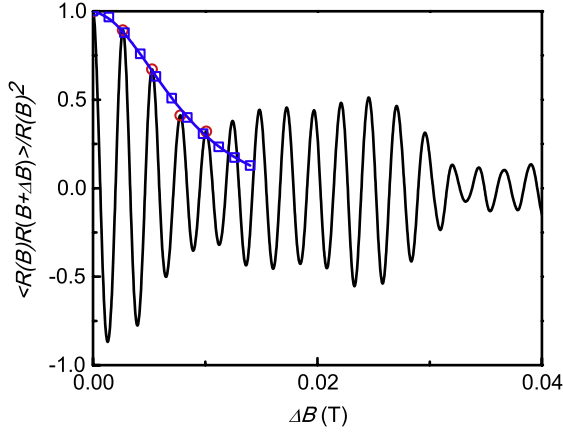
Figure 4. Black solid oscillatory line: the autocorrelation function in B of the Aharonov–Bohm oscillations in figure 3(b). Red open circles $\bigcirc$: the maxima of the autocorrelation function, as a guide to the autocorrelation function envelope. Blue line with open squares $\square$: the fit to the autocorrelation function envelope [21], using the red open circles. The use of a finite range of B leads to deviations between the fit and the data at higher ΔB, as discussed in the text.

recurrently observed as described above, and recently addressed in detail in [12]. In the following we provide two frameworks to understand the modulation of the oscillation amplitude.

Interferometer arms have a finite width w (lithographically in the present study, $w = 300$ nm, while the conducting width is narrower due to the existence of a depletion layer). The conducting arms form a mesoscopic system with properties, such as the complex transmission coefficient, that depend sensitively on the specific realization of the system. When the magnetic flux threading through the interferometer arms $\Phi_c = 2\pi rwB$ varies by $\sim\Phi_0$, a different realization is achieved and the ring's oscillation amplitude and phase are expected to be modified [12, 21]. The autocorrelation function in B of $R(B)$, expressed as $C(\Delta B) = \langle R(B)R(B + \Delta B)\rangle/R(B)^2$, decays according to the accumulated differences in realizations as the applied B varies. Its decay over ΔB, quantified by a correlation field B_c, is expected to form a measure of the magnetic flux necessary to delete correlations between realizations of the interferometer. Figure 4 presents the experimental $C(\Delta B)$ from the data in figure 3(b). Small-period oscillations in $C(\Delta B)$ should agree with the AB oscillation period [21], and indeed the fine oscillations in figure 4(a) show a period of 25 G. When performed on an infinite range of B, the envelope of $C(\Delta B)$ is expected to monotonically reach 0 as ΔB increases. Yet, when performed on data necessarily finite over B, the envelope of the experimental $C(\Delta B)$ is non-monotonic, as figure 4 shows. The envelope [21] is expressed as $C(\Delta B/B_c) \sim (\frac{1}{(2\pi)^2} + \frac{1}{4\sqrt{2}\pi}\frac{\Delta B}{B_c} + \frac{1}{24}(\frac{\Delta B}{B_c})^2)\exp(-\frac{\pi}{\sqrt{2}}\frac{\Delta B}{B_c})$. Only the $\frac{h}{e}$ component is considered in this expression, further valid for $T \to 0$. From figure 4 we deduce a fitted correlation field $B_c = 70$ G. The actual electrically conducting width w_e of the interferometer arms can then be estimated from $w_e = \Phi_0/(2\pi rB_c)$, yielding $w_e \approx 150$ nm. A depletion layer of 75 nm on each side of the arms lies within expectations for ICP-RIE etched
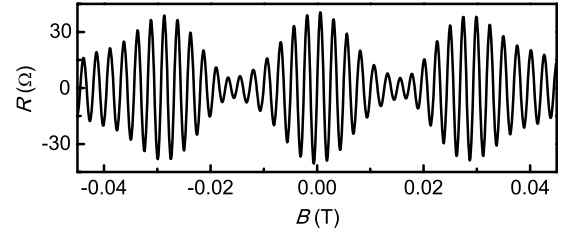

Figure 5. Modulation in the amplitude of Aharonov–Bohm oscillations simulated by using the three discrete frequencies deduced from the Fourier transform in figure 3(c): 376 $1/T$, 408 $1/T$, 447 $1/T$, with intensities 13.2 Ω, 21.6 Ω, 5.89 Ω respectively.

InGaAs 2DESs at the N_S of the measurements. The view of the modulation as resulting from progressively uncorrelated realizations under varying B is hence in accordance with our data.

We now explore whether the quasi-periodic modulation can also be caused by the existence of more than one preferred trajectory through the interferometer arms. In figure 3(c), two minor satellite peaks are noticed around the major $\frac{h}{e}$ Fourier component. The satellites can be interpreted as originating from trajectories deviating from the geometric center of the arms, hence resulting in differing AB fluxes and periods. Careful analysis shows that the central major $\frac{h}{e}$ Fourier component occurs at a frequency 408 $1/T$, while the minor satellite peaks occur at 376 and 447 $1/T$. Using these frequencies and their corresponding intensities, a simplified three-component model is simulated as in figure 5. Comparing figure 5 with 3(b), we note the resemblance, quantified by the observation that the local minimum and local maximum points of the two curves' envelopes almost coincide. Corresponding to 408 $1/T$, 376 $1/T$ and 447 $1/T$, the approximate radii are 734 nm, 704 nm and 768 nm respectively. These radii lie within the ring design. From this approach and using the observation that the fringes to the $\frac{h}{e}$ component in the frequency spectrum extend over a wider range than considered in the simplified calculation, we can deduce that the electrically conducting width w_e must exceed 60 nm. The estimate $w_e > 60$ nm is consistent with the value $w_e \approx 150$ nm deduced from $C(\Delta B)$. While the use of $C(\Delta B)$ provides more quantitative information, both approaches to the amplitude modulation agree that the finite arm width and the resulting variation in magnetic flux can cause the modulation.

3.2. AB oscillations in higher magnetic fields

AB oscillations are observed over a wide range of B. Figure 6 shows a typical measurement with B over -0.6 to 0.6 T. The AB oscillation period is too fine to be resolved on this scale. The AB oscillations occur on a background of universal conductance fluctuations, as well as MR caused by classical size effects. The inset of figure 6 shows a magnified view around 0.57 T, resolving the AB oscillations. At higher B, Shubnikov–de Haas oscillations gradually appear.
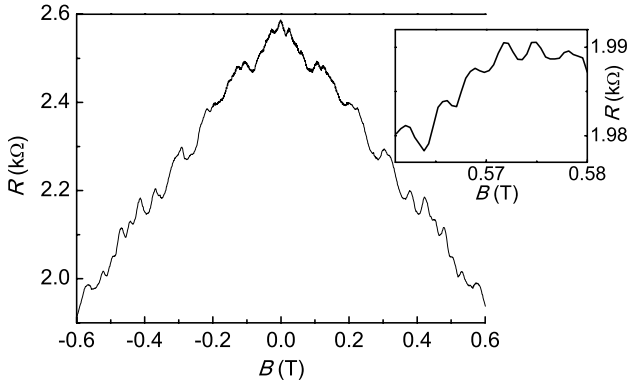
Figure 6. The ring magnetoresistance at 0.4 K over *B* from −0.6 to 0.6 T. The Aharonov–Bohm magnetoresistance oscillations (not fully resolved on the scale of the graph) are superimposed on universal conductance fluctuations. The inset shows a selected narrow range of *B* around 0.57 T to resolve the oscillations.

3.3. The phase coherence length in AB rings

The Fourier spectrum of $R(B)$ can be used to deduce l_ϕ by applying equation (1), as outlined in section 1. Figure 7 demonstrates the process, yielding the value $l_\phi = 3$ μm at $T = 0.4$ K. The low excitation current ($I = 20$ nA rms) and low T used to obtain the data for the fit to equation (1) ensures that distortion of the value of l_ϕ by energy smearing is minimized. The value $l_\phi > l_e = 1.7$ μm shows that, at low T, inelastic phase breaking scattering events will indeed be rarer than elastic momentum scattering events. We note that the phase coherence in our samples is mostly maintained over a length greater than πr, explaining the observation of a strong AB effect. The data from the sample and cooldown depicted in figure 7 show high Fourier components up to $\frac{h}{4e}$. Such high components are not observed in all samples and cooldowns, due to the delicate dependence on unintentional impurity configurations in the mesoscopic sample, as mentioned above. As a contrast, the Fourier transform in figure 3(c) represents data from another sample and cooldown, and shows just two components.

3.4. Current and temperature dependence of the AB oscillations

Transport measurements over the AB rings were performed under constant rms values of the ac excitation currents I and under constant T. To ascertain the bias dependence of the AB oscillation amplitudes, the excitation voltage V_{exc} was calculated for each given I using the known ring resistance (≈ 2.5 kΩ). For the bias dependence study, T was fixed to 0.4 K. For the study of the dependence on T, I was fixed at 20 nA, sufficiently low to achieve a saturation of the measured amplitudes, thereby ensuring that the finite excitation did not distort the results.

Figure 8 shows that the oscillations weaken as I increases. For a detailed study of the relationship between I and the AB oscillation amplitude, we selected a group of ten adjacent periods from 0.01 to 0.04 T, and calculated their mean amplitude. Results using this mean amplitude are depicted in
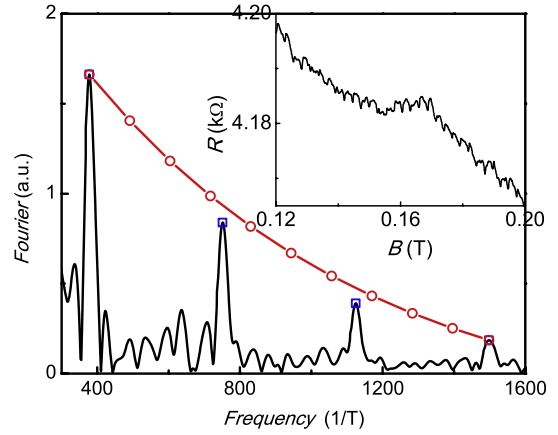

Figure 7. The fit to equation (1) to extract the phase coherence length l_ϕ of the Aharonov–Bohm ring (data from the second sample at 0.4 K). The inset shows the Aharonov–Bohm magnetoresistance oscillations used for the Fourier transform, itself depicted as the black solid line in the main graph. The red line with open circles ◯ depicts the fit to equation (1).
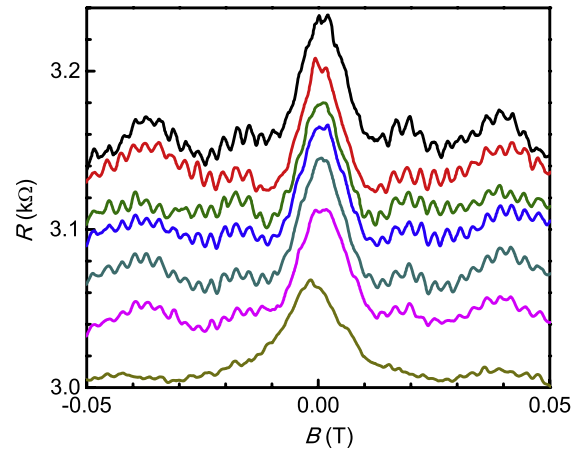

Figure 8. The excitation current dependence of the Aharonov–Bohm magnetoresistance oscillations at 0.4 K (data from the first sample, but with a different cooldown from that for figures 2, 3 and 6). From top to bottom, the excitation current (rms values) is 5 nA, 10 nA, 20 nA, 50 nA, 100 nA, 200 nA and 500 nA respectively. Curves are offset, actual $R(B = 0) \approx 2.5$ kΩ.

figure 9(a). As I increases beyond a threshold, the amplitude overall decreases, but shows a local maximum at ∼50 nA. Such non-monotonic behavior was also observed in other experiments [22], is called the lobe structure, and has been theoretically attributed to electron–electron interactions.

The T dependence is depicted in figure 10, showing a weakening of amplitudes with increasing T. For the analysis the same averaging method was applied as for the dependence on I, with the results contained in figure 9(b). Within experimental uncertainty, the figure shows a mostly monotonic decrease with T.

We notice that variations in I and T do not modify the modulation in B, as can be ascertained from figures 8 and 10. Unlike B, the parameters I and T hence do not induce new realizations of the entire mesoscopic system,
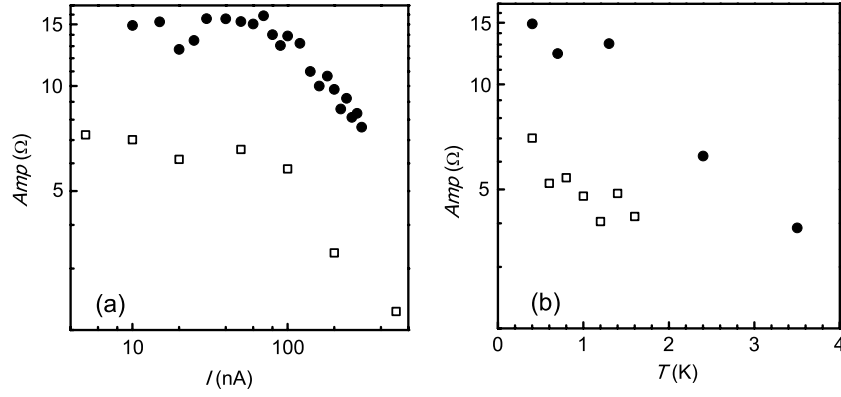
Figure 9. The excitation current and T dependence of the amplitude of the Aharonov–Bohm magnetoresistance oscillations (open squares □ and filled circles ● represent data from the first sample at different cooldowns). Panel (a) shows the excitation current dependence at 0.4 K, with a logarithmic scale on both axes. Panel (b) shows the T dependence at 20 nA, with a logarithmic scale on the vertical axis.
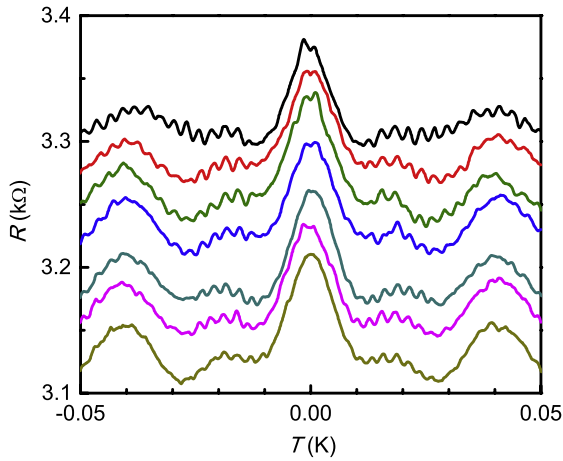

Figure 10. The T dependence of the Aharonov–Bohm magnetoresistance oscillations at 20 nA (data as in figure 8 from the first sample, but with a different cooldown from that for figures 2, 3 and 6). From top to bottom T is 0.4 K, 0.6 K, 0.8 K, 1.0 K, 1.2 K, 1.4 K and 1.6 K respectively. Curves are offset, actual $R(B = 0) \approx 2.5$ kΩ.

4. Conclusions

Pronounced Aharonov–Bohm oscillations are observed in the magnetoresistance of mesoscopic interferometric rings patterned on an InGaAs/InAlAs two-dimensional electron system, with observations spanning a range of magnetic fields, excitation currents and temperatures. The period in the magnetic field of the oscillations matches the Aharonov–Bohm prediction for the design. Fourier transformation is used to discuss the observed modulation of the oscillation amplitude with magnetic field, and to deduce the phase coherence length. The autocorrelation function is used to derive the quasi-period of the amplitude modulation, and both the Fourier transform and autocorrelation function point to the finite width of the interferometer arms as the origin of the modulation. The dependences of the oscillation amplitude on the excitation current and temperature show the existence of critical excitation energies consistent with the Thouless energy scale. Quantum coherence in the mesoscopic interferometers is reduced for thermally or electrically induced excitations beyond the system's Thouless energy, with a concomitant decrease in the Aharonov–Bohm oscillation amplitude.

at least not in the range used in this work. The AB oscillation amplitude decreases caused by I and T can be imputed to energy smearing, discussed above in the context of equation (2), expressing the Thouless energy scale E_c. Using $L = \pi r$ and the 2DES properties, equation (2) predicts an estimate of $E_c = 2.4 \times 10^{-4}$ eV. A critical excitation current I_c can then be estimated by letting $\Delta E(I_c) = E_c$ (with $R = R(B = 0)$), and a critical temperature T_c by letting $\Delta E(T_c) = E_c$ (with $\kappa = 3$). The estimates yield $I_c \approx 100$ nA and $T_c \approx 1.0$ K. When I or T exceed these critical values, averaging over incoherent channels gains in importance and the AB amplitude weakens proportionally to $\sqrt{E_c/\Delta E}$. The data in figure 9 is in accordance with the estimates of the critical values and with the $I^{-1/2}$ and $T^{-1/2}$ behavior predicted by equation (2). For finite mesoscopic systems relying on quantum coherence, such as the interferometric rings studied here, the Thouless energy hence serves as a predictor for loss of coherence.

References

[1] Aharonov Y and Bohm D 1959 *Phys. Rev.* **115** 485
[2] Aharonov Y and Bohm D 1961 *Phys. Rev.* **123** 1511
[3] Washburn S and Webb R A 1986 *Adv. Phys.* **35** 375
[4] Washburn S and Webb R A 1992 *Rep. Prog. Phys.* **55** 1311

[5] Mur L C *et al* 2008 *New J. Phys.* **10** 073031
[6] Lin J J *et al* 2002 *J. Phys.: Condens. Matter* **14** R501
[7] Harmans C 2003 *Mesoscopic Physics, an Introduction* (lecture notes, Delft University of Technology) pp 19, 99, 102
[8] Milliken F P *et al* 1987 *Phys. Rev.* B **36** 4465
[9] Hansen A E *et al* 2001 *Phys. Rev.* B **64** 045327
[10] Edwards J T and Thouless D J 1972 *J. Phys. C: Solid State Phys.* **5** 807
[11] Kurdak C *et al* 1992 *Phys. Rev.* B **46** 6846
[12] Castellanos-Beltran M A *et al* 2013 *Phys. Rev. Lett.* **110** 156801
[13] Morpurgo A F *et al* 1998 *Phys. Rev. Lett.* **80** 1050
[14] Yau J-B *et al* 2002 *Phys. Rev. Lett.* **88** 146801
[15] Yang M J *et al* 2004 *Europhys. Lett.* **66** 826
[16] Webb R A *et al* 1985 *Phys. Rev. Lett.* **54** 2696
[17] Meijer F E *et al* 2004 *Phys. Rev.* B **69** 035308
[18] de Vegvar P G N *et al* 1989 *Phys. Rev.* B **40** 3491
[19] Ford C J B *et al* 1989 *Appl. Phys. Lett.* **54** 21
[20] Nichele J *et al* 2013 *New J. Phys.* **15** 033029
[21] Ginossar E *et al* 2010 *Phys. Rev.* B **81** 155448
[22] Yamauchi Y *et al* 2009 *Phys. Rev.* B **79** 161306